SINTEF
PROCEEDINGS
2

Proceedings of the 12th International Conference on Computational Fluid Dynamics in the Oil & Gas, Metallurgical and Process Industries

Progress in Applied CFD – CFD2017

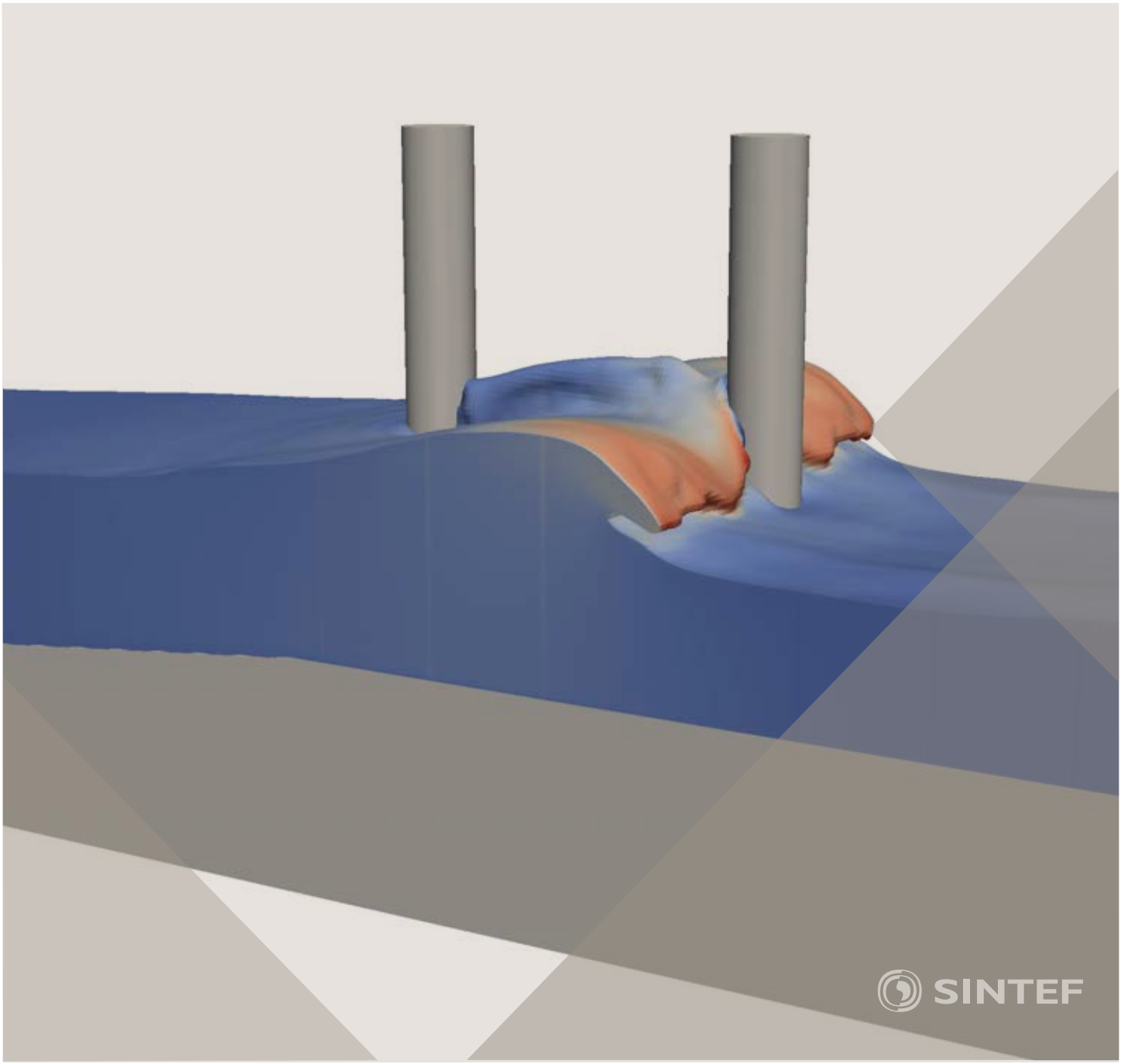

SINTEF Proceedings

Editors:
Jan Erik Olsen and Stein Tore Johansen

Progress in Applied CFD – CFD2017

Proceedings of the 12th International Conference on Computational Fluid Dynamics in the Oil & Gas, Metallurgical and Process Industries

SINTEF Academic Press

SINTEF Proceedings no 2
Editors: Jan Erik Olsen and Stein Tore Johansen
Progress in Applied CFD – CFD2017
Selected papers from 10th International Conference on Computational Fluid Dynamics in the Oil & Gas, Metallurgical and Process Industries

Key words:
CFD, Flow, Modelling

Cover, illustration: Arun Kamath

ISSN 2387-4295 (online)
ISBN 978-82-536-1544-8 (pdf)

SINTEF Academic Press
Address: Forskningsveien 3 B
PO Box 124 Blindern
N-0314 OSLO
Tel: +47 73 59 30 00
Fax: +47 22 96 55 08

www.sintef.no/byggforsk
www.sintefbok.no

SINTEF Proceedings
SINTEF Proceedings is a serial publication for peer-reviewed conference proceedings on a variety of scientific topics.
The processes of peer-reviewing of papers published in SINTEF Proceedings are administered by the conference organizers and proceedings editors. Detailed procedures will vary according to custom and practice in each scientific community.

PREFACE

This book contains all manuscripts approved by the reviewers and the organizing committee of the 12th International Conference on Computational Fluid Dynamics in the Oil & Gas, Metallurgical and Process Industries. The conference was hosted by SINTEF in Trondheim in May/June 2017 and is also known as CFD2017 for short. The conference series was initiated by CSIRO and Phil Schwarz in 1997. So far the conference has been alternating between CSIRO in Melbourne and SINTEF in Trondheim. The conferences focuses on the application of CFD in the oil and gas industries, metal production, mineral processing, power generation, chemicals and other process industries. In addition pragmatic modelling concepts and bio-mechanical applications have become an important part of the conference. The papers in this book demonstrate the current progress in applied CFD.

The conference papers undergo a review process involving two experts. Only papers accepted by the reviewers are included in the proceedings. 108 contributions were presented at the conference together with six keynote presentations. A majority of these contributions are presented by their manuscript in this collection (a few were granted to present without an accompanying manuscript).

The organizing committee would like to thank everyone who has helped with review of manuscripts, all those who helped to promote the conference and all authors who have submitted scientific contributions. We are also grateful for the support from the conference sponsors: ANSYS, SFI Metal Production and NanoSim.

Stein Tore Johansen & Jan Erik Olsen

Organizing committee:

Conference chairman: Prof. Stein Tore Johansen
Conference coordinator: Dr. Jan Erik Olsen
Dr. Bernhard Müller
Dr.Sigrid Karstad Dahl
Dr.Shahriar Amini
Dr.Ernst Meese
Dr.Josip Zoric
Dr.Jannike Solsvik
Dr.Peter Witt

Scientific committee:

Stein Tore Johansen, SINTEF/NTNU
Bernhard Müller, NTNU
Phil Schwarz, CSIRO
Akio Tomiyama, Kobe University
Hans Kuipers, Eindhoven University of Technology
Jinghai Li, Chinese Academy of Science
Markus Braun, Ansys
Simon Lo, CD-adapco
Patrick Segers, Universiteit Gent
Jiyuan Tu, RMIT
Jos Derksen, University of Aberdeen
Dmitry Eskin, Schlumberger-Doll Research
Pär Jönsson, KTH
Stefan Pirker, Johannes Kepler University
Josip Zoric, SINTEF

CONTENTS

PRAGMATIC MODELLING 9
On pragmatism in industrial modeling. Part III: Application to operational drilling 11
CFD modeling of dynamic emulsion stability 23
Modelling of interaction between turbines and terrain wakes using pragmatic approach 29

FLUIDIZED BED 37
Simulation of chemical looping combustion process in a double looping fluidized bed reactor with cu-based oxygen carriers 39
Extremely fast simulations of heat transfer in fluidized beds 47
Mass transfer phenomena in fluidized beds with horizontally immersed membranes 53
A Two-Fluid model study of hydrogen production via water gas shift in fluidized bed membrane reactors 63
Effect of lift force on dense gas-fluidized beds of non-spherical particles 71
Experimental and numerical investigation of a bubbling dense gas-solid fluidized bed 81
Direct numerical simulation of the effective drag in gas-liquid-solid systems 89
A Lagrangian-Eulerian hybrid model for the simulation of direct reduction of iron ore in fluidized beds 97
High temperature fluidization - influence of inter-particle forces on fluidization behavior 107
Verification of filtered two fluid models for reactive gas-solid flows 115

BIOMECHANICS 123
A computational framework involving CFD and data mining tools for analyzing disease in cartoid artery 125
Investigating the numerical parameter space for a stenosed patient-specific internal carotid artery model 133
Velocity profiles in a 2D model of the left ventricular outflow tract, pathological case study using PIV and CFD modeling 139
Oscillatory flow and mass transport in a coronary artery 147
Patient specific numerical simulation of flow in the human upper airways for assessing the effect of nasal surgery 153
CFD simulations of turbulent flow in the human upper airways 163

OIL & GAS APPLICATIONS 169
Estimation of flow rates and parameters in two-phase stratified and slug flow by an ensemble Kalman filter 171
Direct numerical simulation of proppant transport in a narrow channel for hydraulic fracturing application 179
Multiphase direct numerical simulations (DNS) of oil-water flows through homogeneous porous rocks 185
CFD erosion modelling of blind tees 191
Shape factors inclusion in a one-dimensional, transient two-fluid model for stratified and slug flow simulations in pipes 201
Gas-liquid two-phase flow behavior in terrain-inclined pipelines for wet natural gas transportation 207

NUMERICS, METHODS & CODE DEVELOPMENT 213
Innovative computing for industrially-relevant multiphase flows 215
Development of GPU parallel multiphase flow solver for turbulent slurry flows in cyclone 223
Immersed boundary method for the compressible Navier–Stokes equations using high order summation-by-parts difference operators 233
Direct numerical simulation of coupled heat and mass transfer in fluid-solid systems 243
A simulation concept for generic simulation of multi-material flow, using staggered Cartesian grids 253
A cartesian cut-cell method, based on formal volume averaging of mass, momentum equations 265
SOFT: a framework for semantic interoperability of scientific software 273

POPULATION BALANCE 279
Combined multifluid-population balance method for polydisperse multiphase flows 281
A multifluid-PBE model for a slurry bubble column with bubble size dependent velocity, weight fractions and temperature 285
CFD simulation of the droplet size distribution of liquid-liquid emulsions in stirred tank reactors 295
Towards a CFD model for boiling flows: validation of QMOM predictions with TOPFLOW experiments 301
Numerical simulations of turbulent liquid-liquid dispersions with quadrature-based moment methods 309
Simulation of dispersion of immiscible fluids in a turbulent couette flow 317
Simulation of gas-liquid flows in separators - a Lagrangian approach 325
CFD modelling to predict mass transfer in pulsed sieve plate extraction columns 335

BREAKUP & COALESCENCE 343
Experimental and numerical study on single droplet breakage in turbulent flow 345
Improved collision modelling for liquid metal droplets in a copper slag cleaning process 355
Modelling of bubble dynamics in slag during its hot stage engineering 365
Controlled coalescence with local front reconstruction method 373

BUBBLY FLOWS 381
Modelling of fluid dynamics, mass transfer and chemical reaction in bubbly flows 383
Stochastic DSMC model for large scale dense bubbly flows 391
On the surfacing mechanism of bubble plumes from subsea gas release 399
Bubble generated turbulence in two fluid simulation of bubbly flow 405

HEAT TRANSFER 413
CFD-simulation of boiling in a heated pipe including flow pattern transitions using a multi-field concept 415
The pear-shaped fate of an ice melting front 423
Flow dynamics studies for flexible operation of continuous casters (flow flex cc) 431
An Euler-Euler model for gas-liquid flows in a coil wound heat exchanger 441

NON-NEWTONIAN FLOWS 449
Viscoelastic flow simulations in disordered porous media 451
Tire rubber extrudate swell simulation and verification with experiments 459
Front-tracking simulations of bubbles rising in non-Newtonian fluids 469
A 2D sediment bed morphodynamics model for turbulent, non-Newtonian, particle-loaded flows 479

METALLURGICAL APPLICATIONS 491
Experimental modelling of metallurgical processes 493
State of the art: macroscopic modelling approaches for the description of multiphysics phenomena within the electroslag remelting process 499
LES-VOF simulation of turbulent interfacial flow in the continuous casting mold 507
CFD-DEM modelling of blast furnace tapping 515
Multiphase flow modelling of furnace tapholes 521
Numerical predictions of the shape and size of the raceway zone in a blast furnace 531
Modelling and measurements in the aluminium industry - Where are the obstacles? 541
Modelling of chemical reactions in metallurgical processes 549
Using CFD analysis to optimise top submerged lance furnace geometries 555
Numerical analysis of the temperature distribution in a martensic stainless steel strip during hardening 565
Validation of a rapid slag viscosity measurement by CFD 575
Solidification modeling with user defined function in ANSYS Fluent 583
Cleaning of polycyclic aromatic hydrocarbons (PAH) obtained from ferroalloys plant 587
Granular flow described by fictitious fluids: a suitable methodology for process simulations 593
A multiscale numerical approach of the dripping slag in the coke bed zone of a pilot scale Si-Mn furnace 599

INDUSTRIAL APPLICATIONS 605
Use of CFD as a design tool for a phospheric acid plant cooling pond 607
Numerical evaluation of co-firing solid recovered fuel with petroleum coke in a cement rotary kiln: Influence of fuel moisture 613
Experimental and CFD investigation of fractal distributor on a novel plate and frame ion-exchanger 621

COMBUSTION 631
CFD modeling of a commercial-size circle-draft biomass gasifier 633
Numerical study of coal particle gasification up to Reynolds numbers of 1000 641
Modelling combustion of pulverized coal and alternative carbon materials in the blast furnace raceway 647
Combustion chamber scaling for energy recovery from furnace process gas: waste to value 657

PACKED BED 665
Comparison of particle-resolved direct numerical simulation and 1D modelling of catalytic reactions in a packed bed 667
Numerical investigation of particle types influence on packed bed adsorber behaviour 675
CFD based study of dense medium drum separation processes 683
A multi-domain 1D particle-reactor model for packed bed reactor applications 689

SPECIES TRANSPORT & INTERFACES 699
Modelling and numerical simulation of surface active species transport - reaction in welding processes 701
Multiscale approach to fully resolved boundary layers using adaptive grids 709
Implementation, demonstration and validation of a user-defined wall function for direct precipitation fouling in Ansys Fluent 717

FREE SURFACE FLOW & WAVES 727
Unresolved CFD-DEM in environmental engineering: submarine slope stability and other applications 729
Influence of the upstream cylinder and wave breaking point on the breaking wave forces on the downstream cylinder 735
Recent developments for the computation of the necessary submergence of pump intakes with free surfaces 743
Parallel multiphase flow software for solving the Navier-Stokes equations 752

PARTICLE METHODS 759
A numerical approach to model aggregate restructuring in shear flow using DEM in Lattice-Boltzmann simulations 761
Adaptive coarse-graining for large-scale DEM simulations 773
Novel efficient hybrid-DEM collision integration scheme 779
Implementing the kinetic theory of granular flows into the Lagrangian dense discrete phase model 785
Importance of the different fluid forces on particle dispersion in fluid phase resonance mixers 791
Large scale modelling of bubble formation and growth in a supersaturated liquid 798

FUNDAMENTAL FLUID DYNAMICS 807
Flow past a yawed cylinder of finite length using a fictitious domain method 809
A numerical evaluation of the effect of the electro-magnetic force on bubble flow in aluminium smelting process 819
A DNS study of droplet spreading and penetration on a porous medium 825
From linear to nonlinear: Transient growth in confined magnetohydrodynamic flows 831

NUMERICAL ANALYSIS OF THE TEMPERATURE DISTRIBUTION IN A MARTENSITIC STAINLESS STEEL STRIP DURING HARDENING

Pouyan Pirouznia [1, 2, 3], Nils Å. I. Andersson [1*], Anders Tilliander [1], Pär G. Jönsson [1]

[1] Division of Processes, Department of Material Science and Engineering, KTH Royal Institute of Technology, SE-100 44 Stockholm, Sweden

[2] Department of Material Science and Engineering, Dalarna University, SE-791 88 Falun, Sweden

[3] Research & Development Department, voestalpine Precision Strip AB, SE-684 28, Munkfors, Sweden

* E-mail: nilsande@kth.se

ABSTRACT

Due to the increasing demands on higher qualities of thin martensitic steel strips, a great attention needs to be paid to the dimension quality of the finished product within the hardening line. The temperature distribution within the strip during the process influences the flatness of the finished product. Therefore, a FEM model was developed based on physical theories. Specifically, the temperature for the section before martensitic transformation was predicted by using a steady state approach. In addition, the results of the numerical predictions were compared to measured temperature performed in industry by using infrared thermal imaging. The results showed that a significant temperature difference exists across the width of the strip. This difference was 41°C and 48°C at the position close to the bath interface according to the thermal imaging and modelling results, respectively. Furthermore, the temperature measurements showed that the temperature of the strip decreased by 245°C from the furnace temperature within the gas box beyond the hardening furnace. The measurements were performed at a position about 21mm away from the molten metal bath interface. Overall, the results of this study can be seen as initial fundamental knowledge of the modelling of the hardening process. Thereby, this knowledge can be used to modify the current hardening process as well as be used as input to study the stress in strip in future investigations.

Keywords: Process industries, Hardening process, Martempering, Heat transfer, Numerical modelling, Strip.

NOMENCLATURE

Greek Symbols

ρ Mass density, [kg/m^3].
μ Dynamic viscosity, [Pa.s].
ε Emissivity.
γ Specific heat ratio.
σ_b Stefan–Boltzmann constant, [W/ (m^2.K^4)].

Latin Symbols

c_p Heat capacity at a constant pressure, [J/ (kg.K)].
G Incoming radiative heat flux, [W/m^2].
h Heat transfer coefficient, [W/ (m^2.K)].
$\mathbf{I}$ Identity matrix.
k Thermal conductivity, [W/ (m.K)].
p Pressure, [Pa].
T Temperature, [K] unless otherwise stated.
$\mathbf{u}$ Velocity, [m/s].

Sub/superscripts

$^{\mathrm{T}}$ Transpose matrix.

INTRODUCTION

Advanced thin martensitic stainless steel strips, are commonly produced by using a hardening and tempering line or a by using a continuous martempering process. The hardening stage consists of a controlled atmosphere hardening furnace, a martempering media where the strip is cooled to the temperature just above the martensitic transformation, and a finishing step where the strip is quenched to the room temperature. The purpose of the hardening process is to form a desired martensitic structure.

For a conventional batch hardening of a component, hot oils up to 205°C and a molten salts in the range of 160 to 400°C are commonly used as the martempering media (Webster and Laird (1991)). Furthermore, Ebner (1983) indicated that if a molten lead-bismuth eutectic (LBE) alloy is used as a martempering media and afterwards cooled by an air jet, considerable advantages with regards to the flatness can be obtained compared to when using quenching in oil. Later, Lochner (1994) compared different cooling methods such as quenching in a molten metal bath, hydrogen jet and oil and their effects on the flatness of the strip. Later, Lochner (2006) demonstrated the advantages of using a LBE bath as the martempering media when comparing it to various methods of cooling the LBE bath to obtain a natural convection in the media. In addition, the important advantages of selecting LBE as martempering media were summarized, especially with respect to improvements in the flatness and dimensional qualities of the strip.

A LBE bath is used as a media in the continuous hardening process, where mainly: thin strips for springs,

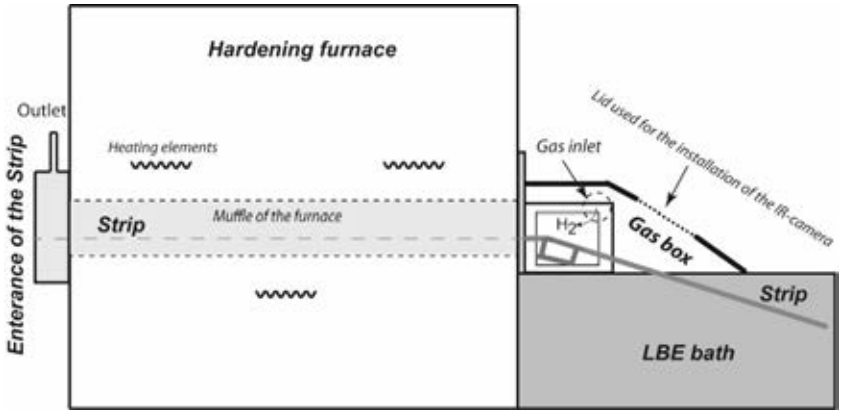

Figure 1: Schematic view of the part of the hardening process which takes place before a martensitic phase transformation at voestalpine Precision Strip AB, Munkfors, Sweden.

blades for the paper & printing industry- and valve steels are produced. A schematic view of the specific hardening process, before the martensitic transformation step, is illustrated in Figure 1. The so called gas box, is a sealing box in which the strip is transported from the muffle of the furnace into the LBE bath. The reducing hydrogen atmosphere of the furnace is provided from the gas inlet located inside the gas box.

Despite all advantages of using LBE as a media in the hardening process, geometrical and flatness defects are still found in the produced strip. In order to investigate how these may form, a better comprehension of the process is required with a focus on the temperature distribution in the strip.

Many researchers referred to the uneven temperature difference as one of the main reasons for the cause of flatness defects. Dimensional changes during case hardening were discussed by Thelning (1984) and he showed that thermal stresses; created during cooling, are the main causes of dimensional changes. In addition, Yoshida (1984) analysed the edge wave of a hot rolled strip after cooling. He established a numerical method to predict the temperature and thermal stresses in the strip. He showed that wavy edges can be removed by using a uniform transverse temperature difference. Wang et al. (1996) studied the deflection problems of the thermomechanical controlled process (TMCP) plates manufactured by the accelerated cooling process. Specifically, the correlation between the temperature variation resulted in thermal stresses and deflections were studied. Different types of flatness deflections, based on the non-uniform cooling in the different directions, were found. Also, Zhou et al. (2007) proved that cooling of a hot rolled strip on the run-out table caused an increased transverse temperature difference between the centre and edges of the strip. This led to an increased buckling tendency. In addition, Wang et al. (2008) showed that uneven transverse temperature distributions in strips are the main reason for flatness defects during a run-out table cooling during rolling of hot steel strips. Furthermore, they developed a numerical model to calculate the amount of thermal stresses that developed during the cooling period. Here, thermal image measurement data across the transverse direction at the exit of the rolling mill were used as the initial conditions in the finite element model (FEM) simulations. Furthermore, model including both thermal and mechanical investigations to predict the flatness of steel strips during the quenching after the last mill stand during hot strip rolling was carried out by Wang et al. (2012). The results by Wang et al. (2013), showed that uneven transverse temperature difference and microstructure differences were the main causes for an edge wave formation of steel strips during the run-out cooling procedure. Moreover, personal communications with experts in the industry (2012), has indicated that the quenching in the molten metal bath has an essential influence on the dimensional attributes of the stainless steel strip.

In spite of all studies regarding the importance of the nature of the temperature on the steel strip quality, very little focus has been put on the temperature distribution of the strip after it leaves the hardening furnace. Therefore, a numerical model was developed which considers the heat transfer of the strip after it leaves the furnace and goes in to the molten metal quenching area. In addition, an infrared thermal imaging camera was used to obtain data to enable validations of the model predictions and to better understand the process. Thus, this study aims to give a better insight into the quenching step in the hardening process as well as to determine the temperature distribution pattern during the cooling of the strip. The results of this study will be used as a base for the investigation of flatness defects in real industrial processes.

MODEL DESCRIPTION

The numerical model was based on the conditions of the hardening process at voestalpine in Munkfors, Sweden. The thermal analysis model was carried out by using Comsol Multiphysics, COMSOL (2015). The focus of the modelling was to study the temperature pattern within the strip as well as in the gas box and the LBE quenching bath.

Mathematical Formulation

The computational model focused on predicting the cooling process of the stainless steel strip and with a specific aim to predict the temperature distribution in the strip. The following assumptions were used in the definition of the numerical model:

I. The laminar Navier-Stokes equation combined with the energy balance and continuity equations were solved numerically for the hydrogen filled gas box domain, where thermal interactions between the strip and the hydrogen gas flow take place.

II. A non-isothermal laminar flow was employed for the hydrogen flow, due to the low Reynolds number of around 485.

III. The Mach number was about 0.00093. Thus, a weak compressibility for the flow was also considered.

IV. Only heat transfer by conduction was considered for the thermal interaction between the strip and the LBE bath.

V. Transient effects (time dependency) were neglected and a steady state solution was chosen for the model simulations.

VI. The gravitational force was neglected.

Based on these assumptions, the following governing equations were solved:

- Continuity equation:

$$\nabla \cdot (\rho \mathbf{u}) = 0 \quad (1)$$

- Momentum equation:

$$\rho \mathbf{u} \cdot \nabla \mathbf{u} = -\nabla p + \nabla \cdot \left(\mu(\nabla \mathbf{u} + (\nabla \mathbf{u})^{\mathrm{T}}) - \frac{2}{3}\mu(\nabla \cdot \mathbf{u})\mathbf{I}\right) \quad (2)$$

- Energy balance equation:

$$\rho c_p \mathbf{u} \cdot \nabla T = \nabla \cdot (k \nabla T) \quad (3)$$

Mesh and the Geometry used in the Numerical Simulation

The geometry of the numerical model was designed based upon the real process conditions. A heated stainless steel strip with a thickness of 0.2mm and a width of 310mm enters the gas box after passing through the hardening furnace. The latter is filled with hydrogen to achieve a reducing atmosphere. Thereafter, a further quenching is provided by the Lead-Bismuth eutectic bath. A schematic view of the three-dimensional solution domain, for which the governing equations were solved, is shown in Figure 2. Furthermore, a complete list of the dimensions used in the mathematical model is given in Table 1.

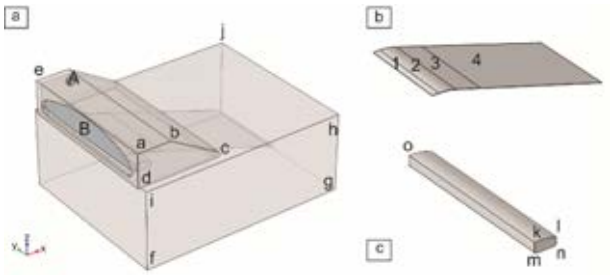

Figure 2: View of computational domains, Length are found in Table 1: (a) three-dimensional solution domains, (b) Stainless steel strip, (c) Gliding material

Table 1: Geometry specifications of the model [mm]. The distances are defined in Figure 2.

Strip (Figure 2b)	1	2	3	4			
	310.0×23.5	310.0×61.3	310.0×97.0	310.0 × 500.0			
LBE bath	$\overline{hi}$	$\overline{fi}$	$\overline{hj}$				
	805.0	300.0	645.0				
Gas box	$\overline{ab}$	$\overline{bc}$	$\overline{cd}$	*$R_{\overline{c}}$	$\overline{ad}$	$\overline{ae}$	
	129.8	222.6	317.6	10	130.0	585.0	
Gliding material (Figure 2c)	$\overline{lm}$	$\overline{mn}$	$\overline{kn}$	$\overline{kl}$	*$R_{\overline{kl}}$	*R_m, R_n	$\overline{ko}$
	15.8	49.0	25.0	59.9	195	5	450.0

R: radius*

The gas box and LBE bath domain correspond to the extrusion of the surfaces of a − d and f − i by the length of $\overline{ae}$ and $\overline{hj}$ in the y-direction respectively. The thickness of the gas box walls is10mm. The gliding material defines the extrusion of k − n by the dimension of $\overline{ko}$ in

Table 2: Boundary conditions used in the model

Surface(s)	*Boundary conditions*	*Expressions*
Inner side of the ceiling of the gas box	• No - slip	$\boldsymbol{u} = 0$
Segments 1-3 of the strip (Figure 2b)	• Moving wall	$\boldsymbol{u_{u,d}} = \boldsymbol{u_{Strip}}$ (<0.17 m/s) $u, d : up, down$
Gas inlet, surface A (Figure 2a)	• Velocity inlet • A Quantified temperature was assumed due to the measured value of the walls of the gas inlet	$3.3\,Nm^3/h$ $(u = 1.18\,m/s \ \ for\ flow\ at\ 200℃)$ $T_A = 200°C$
Surface B and its connected surfaces (Figure 2a)	• A furnace temperature	$T = 1000°C$
Surface B (Figure 2a)	• Pressure outlet (backflow is allowed)	$P_0 = P_{Furnace}$
Outside of the ceiling of the gas box	• Convective heat flux to air (assumed h)	$-k\nabla T = h.(T_{external} - T)$ $T_{external} = 20°C\ ,\ \ h = 0.5\,W/m^2K$
Inner side of the ceiling of the gas box, Surface B (Figure 2a), top surface of segments 1, 2 (Figure 2b), both sides of segment 3 (Figure 2b) of the strip, the surface of the LBE bath in the gas box	• Surface to Surface radiation	$-k\nabla T = \varepsilon.(G - \sigma T^4)$ COMSOL (2015)
Bottom surface of the bath	• Setpoint temperature	$T_{bath} = 300°C$
Top surface of the bath, outside of the gas box	• Convective heat flux to air (Low value of h was assumed due to the surface oxidation)	$-k\nabla T = h.(T_{external} - T)$ $T_{external} = 20°C\ ,\ \ h = 0.1\,W/m^2K$

a mentioned direction as well. The stainless steel strip is shown by the four transverse segments $1-4$ to simplify the adjustment of the boundary conditions, so that they are similar to the industrial process. In addition, the strip was assumed to be a shell due to its thickness. The required hydrogen flow for the hardening furnace is provided from surface A in the gas box ($d_A = 40mm$) and where surface B (Area = 31780mm^2) is specified as an outlet.

According to the complexity of the model, various grid sizes were tested in the model simulations. Specifically the numerical modelling was carried out with three different numbers of elements, i.e. 82310, 289517 and 525884. This was done to improve the calculation time and to achieve mesh-independent results. These meshes contain various amount of grids in the shape of tetrahedral, pyramid, prism, triangular, edge and vertex elements.

Method of solution and boundary conditions

The temperature calculation was based on the consideration of the following statements

I. A heat conduction in the strip.

II. A convective heat transfer within the gas box, i.e. a heat convection between the strip – fluid, fluid – walls of the gas box and the wall of the gas box – the surroundings.

III. A heat radiation, (surface to surface radiation) in the gas box between the surface of the strip, the inner side of the ceiling, and the surface of the LBE bath.

IV. A conduction of heat transfer between the strip and the liquid bath.

The boundary conditions and the initial values used for the numerical model are shown in Table 2, which contains some process-defined values as well as some assumed values. The labels from Figure 2 are used for a clarification of the given values.

Physical parameters used in the model

A chromium stainless steel, uddeholmstrip SS716, was the main target of this study. Its physical parameters used in the model are based on the data sheets of the nearest equivalent steel grade, EN 1.4034 or AISI 420 (Spittel and Spittel (2009)). Also, the physical parameters of the LBE used in the model were based on data from the literature (OECD (2007)) as well as from data from the production of strips. The physical parameters which typically vary with the temperature have an essential influence on the results of the numerical model. Table 3 shows linear relationship of the physical parameters as well as a summary of the material physical parameters for each domain, which are being used in the model. Surface emissivity values of 0.5 and 0.4 were assumed for those parts of the strip that contain higher and lower temperatures, i.e. segments 1 and 2 in Figure 2b, respectively. These values were taken from the literature (Wen (2010)), where it was shown that the value of the surface emissivity increased with an increased temperature for an AISI 420 alloy. In addition, these high emisivities were chosen due to the bright surface of the strip resulting from the reducing atmosphere of the furnace. Also, accurate values of the physical properties for hydrogen were taken from NIST (National Institute of Standard and Technology), which extracted their data from Kunz et al. (2007), Leachman et al. (2009) and McCarty et al. (1981). A regression of the data was made and it is shown for the physical parameters of the hydrogen and the thermal conductivity of gliding material and strip.

Table 3: Physical properties of materials used in the model

	Symbol	*Value(s)*
Strip	k	$10^{-7} \cdot T^2 + 0.0024 \cdot T + 24.817$
	ε	$0.5\,, 0.4$
Wall of the gas box	k	44.5
	ρ	7850
	C_p	475
	ε	$0.4\,, 0.6$
Hydrogen	k	$0.0014 \cdot T^{0.8501}$
	ρ	$24.507/\mathrm{T}$
	C_p	$5.96 \cdot 10^{-11} \cdot T^5 - 2.05 \cdot 10^{-7} \cdot T^4 + 2.76 \cdot 10^{-4} \cdot T^3 - 0.18 \cdot T^2 + 56.8 \cdot T + 7500$
	μ	$2 \cdot 10^{-7} \cdot T^{0.6801}$
	γ	1.40
LBE	k	$3.61 + 1.517 \cdot 10^{-2} \cdot T - 1.741 \cdot 10^{-6} \cdot T^2$
	ρ	$11096 - 1.3236 \cdot T$
	C_p	$159 - 2.72 \cdot 10^{-2} \cdot T + 7.12 \cdot 10^{-6} \cdot T^2$
	ε	0.35
Gliding material	k	$10^{-7} \cdot T^2 + 7 \cdot 10^{-6} \cdot T + 0.0253$
	ρ	350
	C_p	1050

In this study, the wall of the gas box and the gliding material were estimated to be equivalent to those of an AISI 4340 alloy and for a typical high temperature board used in this application, respectively. In addition, a surface emissivity of 0.35 was introduced for a bright surface of molten lead according Trinks et al. (2007). Therefore, this value was assumed for the surface emissivity of the molten metal bath. According to a study by Wen (2010), the surface emissivity of steel varies between 0.4 to 0.7, based on the type of steel and the temperature. In this study, a surface emissivity of 0.6 was assumed for the surface which was defined as an outlet or interface of the gas box and the furnace that, which implies an incoming radiated heat from the furnace. This assumed value is based on the fact that the steel muffle is located inside the furnace, where the strip is hardened. For the inner side of the ceiling with a lower temperature, a value of 0.4 was assumed for the surface emissivity.

TEMPERATURE MEASUREMENT IN THE HARDENING PROCESS

Real process temperature measurements were performed by using a DIAS Infrared thermal imaging camera in order to investigate the accuracy of the finite element model and to achieve a better insight about the temperature distribution across the strip. Measurements were carried out in the temperature range of 300 to 1200°C and using 320×256 pixels. The temperature measurements were performed when the process reached its steady state situation in order to gain consistent results. Also, the measurements were carried out on the segment of the strip, just before it entered the LBE bath. This was due to the limited accessibility at the gas box and the installation limitations of the camera such as its

working temperature. The schematic view of the temporary setup of the process for the measurement is shown by Figure 3. A surface emissivity of 0.4 was set for the camera, which is the same value as was used for the initial condition of the strip in the numerical model within this area.

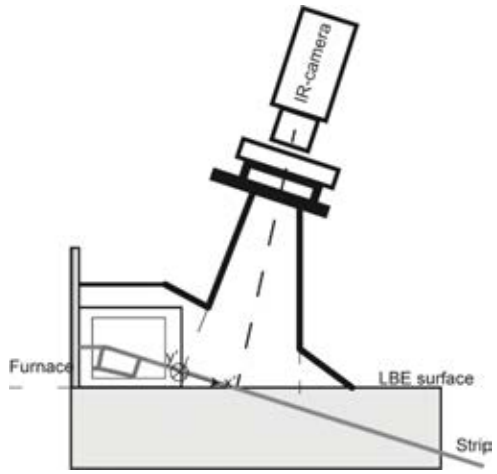

Figure 3: Schematic view of the temporary setup used in the temperature measurement in the industrial hardening process.

RESULTS

Model verification

Three numbers of mesh elements were applied into the FEM model in order to study if mesh-independent results as well as an improved convergence time could be obtained. Also, the temperature distribution across a line in a y-direction (strip's width) with different meshes was investigated and the results are illustrated in Figure 4.

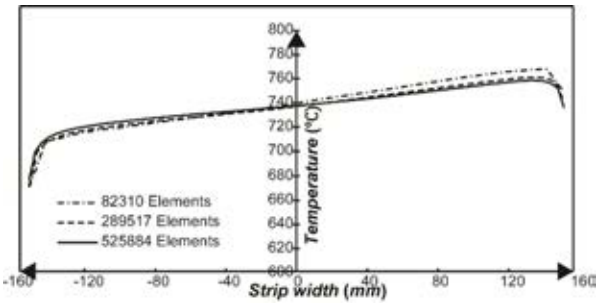

Figure 4: The influence of mesh size on the temperature predictions across the width of strip.

This comparison was done for a line located 63mm before the interface of strip and the bath. The results show that the maximum temperature deviation of the model, meshed with 82310 elements in comparison with the model meshed with 525884 elements is around 1.4%. Furthermore, that this difference decreased to 0.3% when a model with 289517 elements was compared to one with 525884 elements. In addition, the solution time is about 3 times larger when using 525884 elements in comparison to when using 289517 elements. Therefore, the numerical model containing 289517 elements was chosen as the optimum grid for the remaining investigations presented in the current study.

Results of the Computational model

The quenching of a thin stainless steel strip within the hardening line was modelled. In addition, a thermal analysis was performed for the strip in the gas box. Furthermore, the cooling process of the strip within the LBE bath was considered in the model. The hydrogen flow pattern resulting from the computational model of the laminar flow together with its temperature is illustrated in Figure 5.

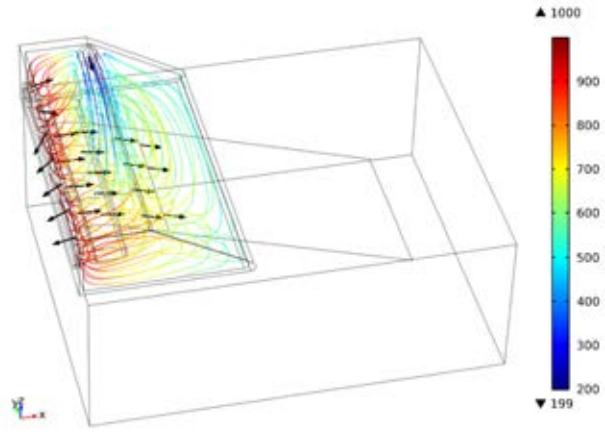

Figure 5: Hydrogen flow pattern and its temperature variation[°C].

As can be seen in this figure, the strip faces a colder flow at the area closest to the inlet. Furthermore, due to a mixture of the fluid and the heat from the strip, a warmer flow is available for the other segments of the strip before its entry to the quenching bath.

The prediction of the temperature pattern for the stainless steel strip was one of the main aims of this project. The temperature distribution within the strip after cooling, caused by the laminar flow and the quenching bath, is shown by Figure 6. The temperature at the exit of the hardening furnace is about 1000°C. However, as it can be seen, this value decreases to about 630°C after cooling by the cold hydrogen flow in the gas box. Also, the temperature drop is more significant on the strip side located nearest to the flow inlet compared to other parts of the strip. A non-uniform temperature distribution within the strip remains visible, especially across its transverse direction in the gas box. Therefore, a uniform temperature pattern is gradually becoming visible after a quenching of the strip by the liquid metal bath.

Figure 7 illustrates the temperature difference across the two edges and the centre of the strip. It can be seen that the strip temperature decreases dramatically from 1000°C to about 630°C before quenching by the molten metal, which occurs at a length of 175mm from the exit of the furnace.

At the position between 50-150mm, it can be seen that the strip at the opposite side of the gas inlet is subjected to less cooling than at the side close to the cold hydrogen gas inflow. Due to this result, the temperature of the strip decreases dramatically to a value of about 681°C. Also, significant transverse temperature difference between the two edges at the introductory part of cooling can be observed explicitly. Specifically, it can be up to about 73°C at the longitudinal position of 93mm. In addition, the centre part of the strip is exposed to the cold flow as well. Therefore, the far edges shows a maximum value of the temperature at the initial part of the cooling zone.

At the area between 150-175mm, the centre part shows a higher temperature value of in comparison to at the edges of the strip. This is caused by the mixture of the gas with the incoming heat from the furnace and the heat from the

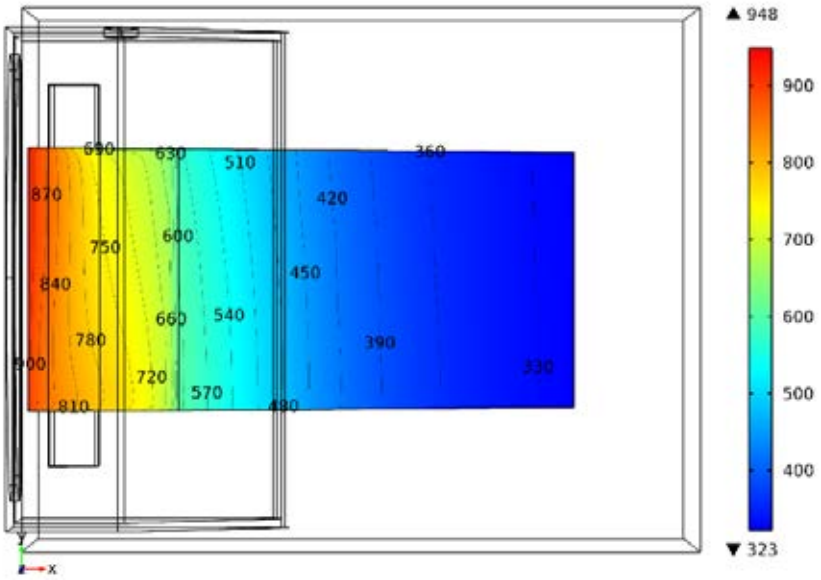

Figure 6: Temperature pattern within the strip [°C].

strip as well as by the three way heat convection at the edges. Therefore, a lower transverse temperature difference can be seen in the further cooling part of the strip. However, as shown in Figure 6, the strip at the area far from the inlet has its warmest area before the quenching by the bath. Also, a non-symmetrical temperature difference is present in the strip.

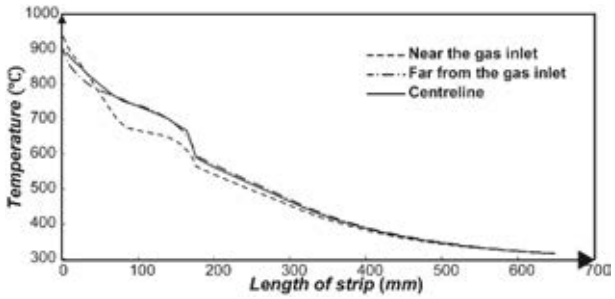

Figure 7: Temperature trajectories across the two edges and at the centre of the strip.

Measured temperatures versus model predictions

A direct comparison of the real process temperature measurement and the predicted result is shown in Figure 8. Figure 8a shows the predicted temperature results from the model at the area where the real process temperature measurements had been carried out. Moreover, a result of the measured temperature done by the infrared thermal imaging camera is shown in Figure 8b. GS stands for the gas inlet side at which the inflow of gas is located in the gas box and OS defines the Operator side. Two straight lines named *I-I* and *II-II* were used for the validation of the numerical model across the transverse and along the longitudinal direction respectively. According to the thermal image analysis, the strip is slightly buckled at the entry of the quenching by the LBE bath. As shown in Figure 8, the same tendency of the transverse temperature distribution can be seen in both the measured and predicted results. It has been shown that the area located furthest from the gas inlet had the highest temperature in comparison to the other positions.

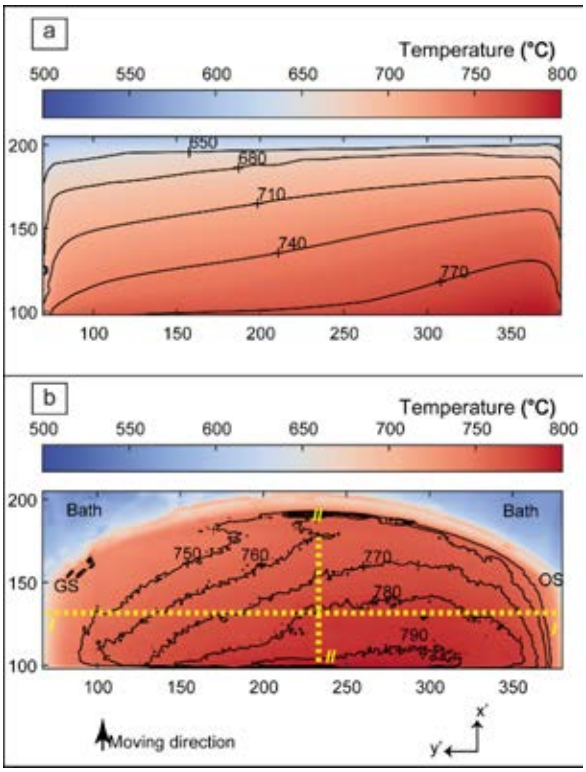

Figure 8: Temperature results (a) Predicted result from the numerical model, (b) A result from the measurements using the infrared thermal imaging camera to measure the temperature distribution on the strip

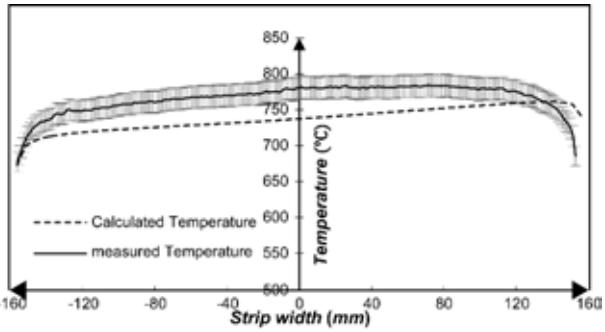

Figure 9: Comparison between the result of the predicted and measured temperatures across the width of strip, where line *I-I* is defined in Figure 8.

A Comparison of the numerical calculation results and measured temperature distribution across the strips' transverse direction, line *I-I* in Figure 8, is shown in Figure 9. This comparison was done at a position about 63mm from the bath interface. However, it was quite complicated to define the same line for the thermal image analysis and the model. In addition, a ±2% of measured value was considered as the measurement uncertainty of the camera, based on the information given by the manufacturer (DIAS). This uncertainty is shown as an error bar in the diagram. The deviation between the calculated results and the real process data for the maximum temperature is 2.9%. However, the deviation for the minimum temperature is 0.6%. Also a significant transverse temperature difference is visible across the strips width. Specifically, this value was 107°C and 88°C for the measured temperatures and the model predictions, respectively. At the centre of the strip, the deviation between the predicted temperature and the measured value is 5.5%. Furthermore, a cooling at the edges can be seen from the predictions and measured results.

The temperature distribution along the strip's longitudinal direction, line *II-II* in Figure 8, is shown in Figure 10.

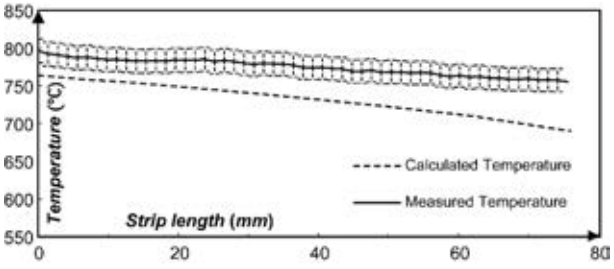

Figure 10: Temperature distribution along the strip's longitudinal direction, where line *II-II* is defined in Figure 8.

The length of the assumed line is about 76mm and it ends at a position about 21mm away from the bath interface. A definition of the exact line with the same position in the model and the thermal image can be identified as the limitation in this specific comparison. The same relationship for the temperature distribution is also found between the model predictions and the measured camera values. Also, the temperatures within the assumed line decrease by about 41°C and 73°C according to the temperature measurement and the model prediction, respectively. This result indicates that a cooling of the strips occur as it passes the gas box. By using a thermal image analysis and model predictions, it can be seen that the temperature of the strip dropped significantly within the gas box before a further quenching by the liquid metal bath took place. Specifically, the temperature of the strip decreased from 1000°C and the furnace temperature to about 755°C and 690°C, according to the thermal analysis and the model results, respectively.

DISCUSSION

The object of this research was to study the quenching process of a thin stainless steel strip within the hardening line. Numerical simulations and empirical temperature measurements by using infrared thermal imaging were performed. The precision of the temperature distribution is an essential parameter to know in order to achieve an accurate comparison between the results of the model predictions and the measured temperatures. In addition, accurate temperature measurements can assist in future investigations of thermal stresses analyses of strips. For instance, Wang et al. (2008) used measured data from the real process as its initial condition parameters for residual stress calculations in steel strips.

According to the results achieved by the numerical model in Figure 6 and Figure 7, the temperature of the strip drops significantly within the gas box. This is due to the existence of a hydrogen flow. The gas inflow in the box was preliminary designed to provide a reducing atmosphere in the hardening furnace. However, a high cooling effect on the stainless steel strip was also observed. Also, a stronger cooling effect has been seen at the area near to the cold gas flow inlet compared to the other parts of the furnace. This resulted in a distinguishable non-uniform temperature distribution within the strip, especially across its transverse direction. Regarding the various cooling conditions of the strip, a drop of the temperature at the edges is not avoidable. This phenomenon was also shown by Suebsomran and Butdee (2013) and Wang et al. (2008) in the cooling process modelling of strip steel on a run-out table in a hot rolling process, where the strip was quenched by an external fluid.

The trajectories of the temperature measured empirically and a comparison with the results of the numerical predictions are shown in Figure 9 and Figure 10. From this comparison, it can be seen that the warmest area of the strip is located at the area away from the gas inlet. Moreover, a significant transverse temperature difference (y-direction) can clearly be observed. The variation of the temperature values between the measured and the model data can be due to the limitations of each approach and due to an error in the comparison method.

A location of an assumed line for the investigation of temperature pattern within the prediction model and the thermal image analysis was performed as good as possible, but it was not perfect. Therefore, it may be difficult to consider precise values of the temperature, as a main target of a comparison. This limitation can also be called a potential error in the comparison of the results.

Various parameters can influence the results of the thermal image results. To obtain a precise value of the measured temperature in the closed gas box is an enormously hard task to achieve. As described in the literature by Minkina and Dudzik (2009), errors in an IR cameras' temperature measurement can be classified into the following reasons: errors of method, calibration errors, and electronic path errors. Many parameters cause errors in the method, which in turn cause a deviation from the actual value of the measured temperature. The following reasons can result in an error of the measuring method; i) an incorrect value of the emissivity of the object, ii) an influence of the ambient radiation which arrives to the detector of the camera directly or that is reflected by the surface of the object, and iii) the atmospheric temperature. Therefore, the definition of the surface emissivity value has an essential influence on the measurements. The object emissivity depends on the temperature of the material, the state of the surface, and the direction of observations (Minkina and Dudzik (2009)).

One of the main primary settings for the thermal imaging camera surface is the surface emissivity of the object. Furthermore, this parameter changes by the temperature of the strip (Wen (2010)). The real process temperature measurements showed that there is about a 4% temperature difference between the values resulting from surface emissivity values of 0.3 and 0.4. Therefore, the setting of a reliable surface emissivity for the whole object area is a quite hard task to perform, since colder areas are located near the edges. In addition, the curved shape of the strip in the LBE bath contact surface imply a buckling of the strip in the gas box. This incident influences the measured temperature of the strip on the top surface and the edges as well by means of changes in the state of the surface.

According to the lens variant of the IR-camera, the camera should be installed at the specific height to obtain accurate measurements. This height is defined based on the HFOV and VFOV, namely the Horizontal Field Of View and Vertical Field Of View, respectively. An implied buckled strip at the area before quenching by the bath, affects these two parameters by changing the height of the camera and the angle of the imaging to the strip. Consequently, this phenomenon causes errors in temperature measurements as well as reflections. This means that the mentioned uncertainty percentage of the measurements and errors caused by a variation of the surface emissivity can be increased.

The calibration error of the camera is ±2% of the measured value according to the manufacturer (DIAS). This parameter is considered as the accuracy when operating the camera under specified laboratory conditions for a black body radiator and for an ambient temperature of 25°C (DIAS). In practical measurements, this uncertainty may be significantly higher (Minkina and Dudzik (2009).

The errors in the electronic path of camera are below ± 1 % for the ambient temperature. For non-contact temperature measurements by infrared cameras, errors in the method are generally the main source of uncertainty, which even can reach values of up to several percent (Minkina and Dudzik (2009)).

Therefore, these limitations can explain the differences between the measured data and calculated values in Figure 9. Therefore, by neglecting the temperature values at the edges (20mm from each side), the maximum value of the temperature for the measured data and the calculated result are 784°C and 761°C, respectively. However, there is about a 62mm difference between their locations. Moreover, the minimum values were 743°C and 713°C. The transverse temperature difference (y-direction), between the maximum and minimum values, at the assumed line in the thermal imaging process is about 41°C. However, this value is increased to 48°C in the numerical predictions. These values stand for a correct conformity between the measured temperatures and the numerical results.

Limitations in the model should always be considered in the comparison of the results with the measured temperatures. The current complex heat transfer model contains many boundary conditions based on the real process. Also, many material parameters also vary with the temperature. Physical parameters, used in the model, were chosen to be as accurate as possible. However, it is still an enormous struggle to find a precise value and a temperature correlation for all the parameters of the different domains. In addition, fluid flow investigations were performed for a hydrogen flow in the gas box and the conduction was the only physics which was considered for the metal quenching bath. Therefore, due to the complexity of the model, the movement of the strip in the LBE bath were not considered. Moreover, to quantify the difference in the measured temperature and the model results in Figure 10, further investigations focusing on the heat convection in the bath are necessary.

CONCLUSIONS

In this study, a thermal analysis numerical model was established and thereafter utilized to investigate the temperature distribution within the molten metal quenching step of a hardening process. Predicted temperatures of the strip were compared to real process thermal measurements using an infrared camera thermal imaging technique. The conclusions of this study may be summarized as follows:

1. The computational model results gave a better insight into the hardening process and a description of the temperature distribution within the quenching step in various domains. A hydrogen flow pattern within the gas box was revealed, which contributes to a better understanding of the temperature distribution on the strip.
2. An infrared thermal imaging used in this study exposed the temperature difference on the strip just before quenching. In addition, a buckled surface of the strip was revealed by these measurements.
3. The surface emissivity had the strongest influence on the results as the initial parameter for the temperature measurement analysis. There was a 4% temperature variation between the results from surface emissivity values of 0.3 and 0.4. Therefore, a calibration of the camera by using different surface emissivity values is suggested in future studies.
4. It has been proven that the strip faced a stronger cooling effect at the area close to the gas inlet, which resulted in a significant transverse temperature. Based on the literature data, extreme temperature difference across the transverse direction can be the source of flatness defects found within the strip.
5. By neglecting the temperature values at the edges (20mm from each side), the transverse temperature differences (y-direction) are about 41°C and 48°C in the real process measurements and the numerical predictions, respectively. Also, the mathematical model showed the same tendency for the temperature distribution within the strip in comparison to the thermal image analysis results. Therefore, the numerical model is deemed to be valid to be used for predictions of temperature distributions in strips.
6. The temperature of the strip, decreases dramatically within the gas box, between the exit of the hardening furnace and the entry of the quenching bath. The temperature of the strip, at 21mm from the bath interface, after the furnace decreased from 1000°C to about 755°C and 690°C according to the thermal analysis and the model results, respectively. It can be concluded that the hydrogen gas flow has a significant cooling effect on the strip, even though it

was preliminary designed to provide a reducing atmosphere in the hardening furnace. Therefore, a change of the gas inlet location might reduce temperature difference across the width of the strip.

7. This study can be used as a fundamental knowledge base for further investigations regarding the thermal stresses caused from non-uniform transverse temperature difference in the quenching step of the hardening process. This, in turn, will help to reduce the flatness problems in industrial hardening processes.

ACKNOWLEDGMENTS

The authors would like to thank Mr. Chris Millward and Mr. Stellan Ericsson of voestalpine Precision Strip AB, for the fruitful discussion and great support with the temperature measurements as well as Mr. Nihat Palanci of Snesotest, Sweden to provide the possibility to use the Infrared camera for the industrial measurements. This study was carried out with a financial support from the Regional Development Council of Dalarna, Regional Development Council of Gävleborg, County Administrative Board of Gävleborg, the Swedish Steel Producers' Association, Dalarna University, Sandviken Municipality and voestalpine Precision Strip AB.

REFERENCES

(2012). Personal communication with Mr. Stellan Eriksson, R&D process technology, voestalpine precision strip AB, Munkfors, Sweden

COMSOL, www.comsol.com/release/5.1, date of access 2017-02-22, Heat Transfer Module User's Guide, Version 5.1, (2015).

DIAS, PYROVIEW 320N, www.dias-infrared.com/pdf/pyroview320n_eng_mail.pdf, date of access 2017-02-22.

Ebner, J., (1983) , "Bright Heat Treating of Carbon Steel Strip Using a Lead Quench", Mach. Steel Austria, 4.

Kunz, O., Klimeck, R., Wagner, W., Jaeschke, M., (2007), "The GERG-2004 Wide-Range Equation of State for Natural Gases and Other Mixtures", GERG Technical Monograph 15 and Fortschr.-Ber., VDI-Verlag, Düsseldorf.

Leachman, J.W., Jacobsen, R.T., Penoncello, S.G., Lemmon, E.W., (2009), "Fundamental Equations of State for Parahydrogen, Normal Hydrogen, and Orthohydrogen", *J. Phys. Chem. Ref. Data*, **38**, 721-748.

Lochner, H., (1994), "Hardening of strip in a molten-metal bath or hydrogen jet cooler", *Steel Times*, **222**, 350.

Lochner, H., (2006), "Steel strip hardening and tempering lines for medium and high carbon steels and alloyed grades part I: Production lines with liquid metal quenching", *Proc. IFHTSE - Int. Fed. Heat Treat. Surf. Eng. Cong.2006*. ASMET, Vienna, 43.

McCarty, R.D., Hord, J., Roder, H., (1981), "Selected properties of hydrogen (engineering design data)", National Engineering Lab (NBS), Boulder, CO (USA).

Minkina, W., Dudzik, S., (2009), "Errors of Measurements in Infrared Thermography, Infrared Thermography", John Wiley & Sons, Ltd, New Jersey, 61.

OECD NEA. Nuclear Science Committee, (2007), "Handbook on Lead-bismuth Eutectic Alloy and Lead Properties, Materials Compatibility, Thermal-hydraulics and Technologies", OECD Nuclear Energy Agency, France, 25.

Spittel, M., Spittel, T., (2009), "Metal Forming Data of Ferrous Alloys - deformation behaviour", Springer Berlin Heidelberg, Berlin, 588.

Suebsomran, A., Butdee, S., (2013), "Cooling process on a run-out table by the simulation method", Case stud. *therm. eng.* **1**, 51-56.

Thelning, K.-E., (1984), "Steel and its Heat Treatment", Second Edition ed. Butterworth-Heinemann, Oxford, 581.

Trinks, W., Mawhinney, M.H., Shannon, R.A., Reed, R.J., Garvey, J.R., (2007), "Industrial Furnaces", John Wiley & Sons, Inc., New Jersey, 190.

Wang, S.-C., Chiu, F.-J., Ho, T.-Y., (1996), "Characteristics and prevention of thermomechanical controlled process plate deflection resulting from uneven cooling", *Mater. Sci. and Technol.* **12**, 64-71.

Wang, X.-d., Li, F., Jiang, Z.-y., (2012), "Thermal, Microstructural and Mechanical Coupling Analysis Model for Flatness Change Prediction During Run-Out Table Cooling in Hot Strip Rolling", *J. Iron Steel Res. Int.*, **19**, 43-51.

Wang, X., Li, F., Yang, Q., He, A., (2013), "FEM analysis for residual stress prediction in hot rolled steel strip during the run-out table cooling", *App. Math. Model.*, **37**, 586.

Wang, X., Yang, Q., He, A., (2008), "Calculation of thermal stress affecting strip flatness change during run-out table cooling in hot steel strip rolling", *J. Mater. Proc. Technol.*, **207**, 130-146.

Webster, H., Laird, W.J., (1991), "ASM Handbook", ASM International, 137-151.

Wen, C.-D., (2010), "Investigation of steel emissivity behaviors: Examination of Multispectral Radiation Thermometry (MRT) emissivity models", *Int. J. Heat and Mass Transf.*, **53**, 2035-2043.

Yoshida, H., (1984), "Analysis of Flatness of Hot Rolled Steel Strip after Cooling", *Trans. Iron Steel Inst. Jpn.*, **24**, 212-220.

Zhou, Z., Lam, Y., Thomson, P.F., Yuen, D.D.W., (2007), "Numerical Analysis of the Flatness of Thin, Rolled Steel Strip on the Runout Table" *Proc. Inst. Mech. Eng., B J. Eng. Manuf.*, **221**, 241-254.